Applied Physics A (2022) 128:1103
https://doi.org/10.1007/s00339-022-06244-y

Applied Physics A
Materials Science & Processing

Structural, morphological and magnetic properties of hexaferrite $BaCo_2Fe_{16}O_{27}$ nanoparticles and their efficient lead removal from water

M. M. Arman[1]

Received: 3 July 2022 / Accepted: 11 November 2022 / Published online: 22 November 2022

Abstract
W-hexaferrite $BaCo_2Fe_{16}O_{27}$ was prepared using the citrate nitrate combustion method. The sample was characterized using XRD, SEM, EDX and elemental mapping. XRD confirmed that the sample was synthesized in a single phase hexagonal structure with an average crystallite size 37.39 nm. SEM images of the sample show a spongy morphology with the agglomerated grain owing to dipole interaction between the crystallites. The magnetic properties of $BaCo_2Fe_{16}O_{27}$ were studied using H-M hysteresis loop and the DC magnetic susceptibility. The sample has a ferrimagnetic behavior with saturation magnetization 64.133 emu/g. The magnetic properties of $BaCo_2Fe_{16}O_{27}$ are originated from the Fe^{3+}–O–Fe^{3+} superexchange. The synthesized sample is used as an adsorbent to remove the heavy metal Pb^{2+} from water. $BaCo_2Fe_{16}O_{27}$ has Pb^{2+} removal efficiency 99% and 28% at pH 8 and 7 respectively. The Langmuir and Freundlich isotherms were used to analyze the experimental data. The Freundlich adsorption isotherm fitted the experimental data well.

Keywords $BaCo_2Fe_{16}O_{27}$ · Hexaferrite · Nanoparticles · The removal efficiency

1 Introduction

The hexaferrites have six main types (*M*-, *U*-, *W*-, *X*-, *Y*- and *Z*-types) according to the chemical formulas and stacking sequences of these building blocks. W-type hexaferrites have a general formula $AMe_2Fe_{16}O_{27}$, where *A* is an alkaline earth ion (i.e., Ba and Sr) and Me is a divalent transition metal ion such as Mg, Zn, Co, Ni, Fe. They are characterized by ferrimagnetic behavior with high Curie temperatures. The magnetic properties of $Ba(Sr)M^{2+}Fe_{16}O_{27}$ vary with the type divalent cation. The hexagonal ferrites are used in a wide range of devices, such as magnetic recording media, high-performance microwave-absorbing, permanent magnets, shielding materials in electronic devices operating at GHz frequencies and bubble memories and microwave devices [1–4].

To unravel the verities of application, various divalent and trivalent cations are frequently inserted in the sub lattices of W-type barium hexagonal ferrites (BHF). Several methods of preparation were used to prepare BHF compounds with different nanocrystal sizes, shapes, and characteristics [5]. The synthesize routes such as the conventional solid-state reaction method [6], the sol–gel method [7], the micro-emulsion route [8], the ball milling [9], auto-combustion [10] and co-precipitation method [11] were used for preparation nanoparticles of BHF systems. The citrate combustion method is a fast, simple and easy technique for the synthesis of a variety of advanced nanomaterials and ceramics [12]. In this method, the thermal redox reaction occurs between an oxidant and a fuel (as citric acid) [13]. The monophasic nanopowders were prepared with a homogeneous microstructure in short reaction times using a citrate combustion method [14, 15].

The structural, morphological and magnetic properties of Ba W- type hexaferrite (BHFs) were strongly influenced by the divalent cations and rare-earth substitution. The enhancement of zinc in $Ba_1Cu_{2-x}Zn_xFe_{16}O_{27}$ ($x=0.0$ and 0.4) has been studied by R. Sagayaraj [5]. The pure and doped samples have a semiconductor like behavior.

The SEM images reveal that the Ba hexaferrites gained the hexagonal structure with spongy morphology. $Ba_1Cu_{2-x}Zn_xFe_{16}O_{27}$ nanoparticles may be utilized

✉ M. M. Arman
mmarmsci@gmail.com; mmarmsci@cu.edu.eg

[1] Materials Science Laboratory (1), Physics Department, Faculty of Science, Cairo University, Giza, Egypt

for treating bacterial infection in the clinical sector. Kai Huang et al. [16] studied the effect of Ca ions on the structure and magnetic properties of BHFs. The samples $Ba_{1-x}Ca_xCo_2Fe_{16}O_{27}$ ($x=0$, 0.1, 0.3, 0.4 and 0.5) were prepared using a sol–gel method. The coercive field and the saturation magnetization were increased by increasing the amount of Ca substitution. The Ca^{2+} doped W- type hexaferrite improved microwave absorbency. M.A. Ahmed et al. [17] studied the effect of the influence of rare-earth ions on the magnetic properties of barium hexaferrite $Ba_{0.95}R_{0.05}Mg_{0.5}Zn_{0.5}CoFe_{16}O_{27}$ (R = Y, Er, Ho, Sm, Nd, Gd, and Ce ions). The curie temperature (T_C) and effective magnetic moment increased for the Sm doped sample. Jin Tang et al. [18] were prepared $Ba_{1-x}La_xFe_2^{2+}Fe_{16}^{3+}O_{27}$ using the standard ceramic method. The values of the lattice constant c decreased with the increase of the doped La^{3+} in the samples. There is a monotonic dependence of the coercivity (H_c) and the magnetic anisotropy field (H_a) on the La^{3+} amount.

Heavy metals in aqueous solutions, such as Cr(VI), Pb(II), and Cd(II), are poisonous even in low amounts and have caused serious health effects on humans. As a result, it is critical to remove these heavy metals from the aqueous environment to protect biodiversity, hydrosphere ecosystems, and humans. To remove these harmful heavy metals from wastewater, several techniques such as chemical precipitation, electrolytic separation, membrane separation, ion exchange, and adsorption have been used [19].

For the removal of heavy metals, the adsorption technique has been widely used. Nanomaterials have been considered an excellent adsorbent for the removal of heavy metal ions from wastewater [20–22]. Nanomaterials were used for removal of heavy metals from water using adsorption techniques based on the physical interaction between metal ions and nanomaterials [23].

In this present work, the author synthesized $BaCo_2Fe_{16}O_{27}$ nanoparticles using the citrate combustion method as a fast, simple and easy technique. The aim of this study is understanding the crystallite structure, morphology and magnetic properties of W-type hexaferrites, additionally, studying the heavy metal removal efficiency using $BaCo_2Fe_{16}O_{27}$ nanoparticles. To identify the best conditions for heavy metal Pb^{2+} ion removal from water, the removal efficiency of Pb^{2+} ion was studied as a function of contact time and pH.

2 Experimental techniques

2.1 Preparation of nanoparticles

The hexaferrite $BaCo_2Fe_{16}O_{27}$ sample was prepared by citrate nitrate combustion method as illustrated in Fig. 1. The metal nitrates (purity 99.9%, Sigma–Aldrich) were mixed in stoichiometric ratios.

2.2 Measurements

The X-ray diffraction (XRD) was carried out using X-ray diffraction (XRD, Bruker advance D8 diffractometer, $\lambda = 1.5418$ Å). The sample was characterized by scanning electron microscopy (SEM) and energy dispersive spectroscopy (EDS) to study the surface morphology and the chemical structure using OXFORD INCA PentaFETX3-England. The magnetic properties of the hexaferrite $BaCo_2Fe_{16}O_{27}$ sample were assessed using two techniques: the first is the H-M hysteresis loop using the vibrating sample magnetometer (VSM; 9600-1 LDJ, USA). While the other is the measurement of the DC magnetic susceptibility as a function of absolute temperature using the Faraday method [24].

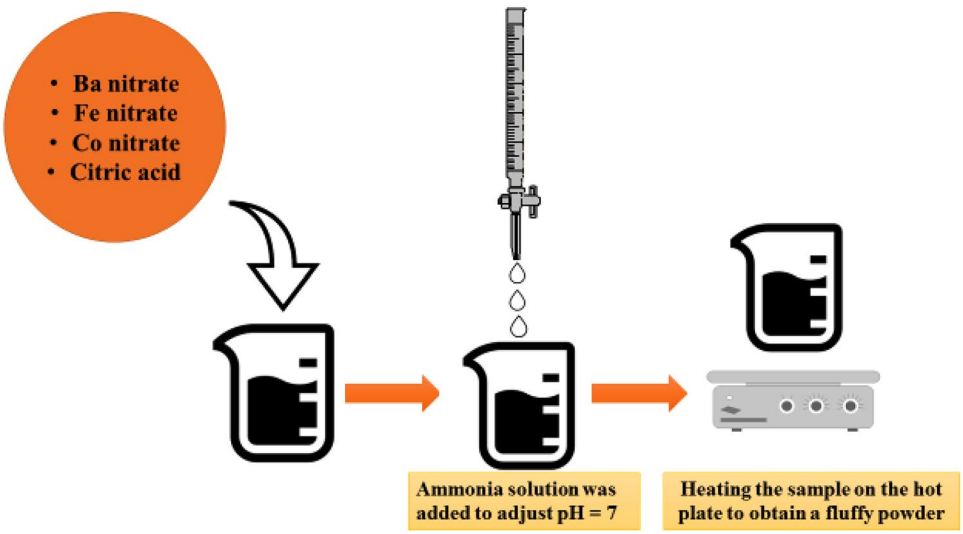

Fig. 1 Flowchart for the synthetic $BaCo_2Fe_{16}O_{27}$

2.3 Heavy metal removal

2.3.1 Effect of pH value

The heavy metal Pb^{2+} ion removal efficiency of $BaCo_2Fe_{16}O_{27}$ sample was studied. Pb^{2+} ions solution of concentration (50 ppm) was prepared as an initial concentration. 0.02 g of $BaCo_2Fe_{16}O_{27}$ nanoparticles was added to five beakers (250-mL) containing the above solution. The pH values of the solutions were adjusted from 3 to 8 and they were stirred using an electric shaker (ORBITAL SHAKER SO1) at 200 rpm for 1 h. A 0.2-m syringe filter was used to filter 10 ml of the supernatant solutions at regular intervals. Inductively coupled plasma (ICP) spectrometry (Prodigy7) was used to determine the concentration of heavy metals in the filtrate.

2.3.2 Effect of contact time

The 50 ppm Pb^{2+} solution was pipetted into a beaker containing 0.10 g of $BaCo_2Fe_{16}O_{27}$, with the pH value adjusted to its optimal value. After varying contact times, the concentration of Pb^{2+} in the solution was determined. The following equations were used to calculate the metal ion removal efficiency (η) and the equilibrium adsorption capacity (q) [25]:

$$\eta = \frac{C_i - C_e}{C_i} \times 100 \tag{1}$$

$$q = \frac{(C_i - C_e)V}{m} \tag{2}$$

where C_i and C_e are the initial and final concentrations (mg/L) of metal ion solution, respectively. While m is the mass of adsorbent and V is the volume of Pb^{2+} solution.

3 Results and discussion

Figure 2 illustrates the XRD pattern of $BaCo_2Fe_{16}O_{27}$ nanoparticles. The sample has a single phase hexagonal structure with the space group $P6_3/mmc$ [5]. The data were indexed with ICDD card number 019–0098. The average crystallite size was calculated using the well-known Debye-Scherer equation formula [26]

$$D = \frac{0.94\lambda}{\beta\cos\theta} \tag{3}$$

where D is the average crystallite size, λ is the wavelength of X-ray radiation, θ is the Bragg angle, and β is the full-width at half-maximum intensity of the powder pattern peak. The average crystallite size is 37.39 nm. The lattice parameters

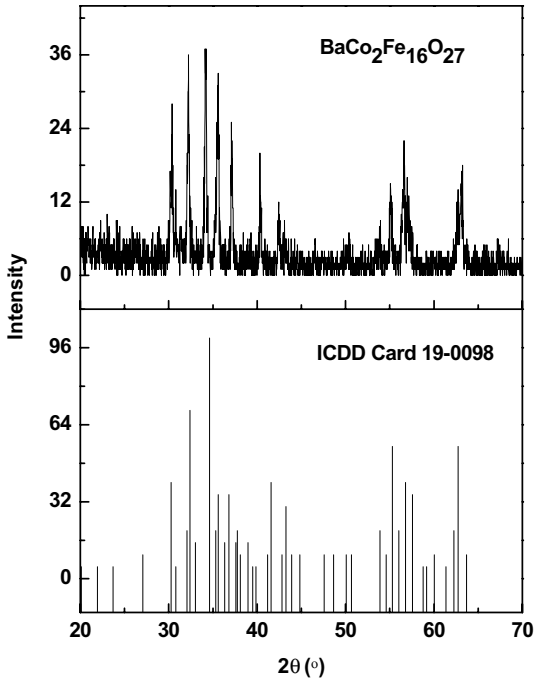

Fig. 2 XRD of the sample $BaCo_2Fe_{16}O_{27}$

were calculated based on the hexagonal symmetry according to Eq. (4).

The value of theoretical density was calculated from Eq. (5) and reported in Table 1

$$D_x = \frac{ZM}{NV} \tag{5}$$

where $Z = 2$ is the number of molecules per unit cell, N is Avogadro's number, M is the molecular weight and V is the unit cell volume [27].

The crystal axis ratio c/a is normally 4.0 for W type Ba hexaferrites. While the value of c/a ratio is 4.6733 for the investigated sample, owing to the migration of divalent cations in the voids causes the John–Teller effect [5].

The morphology and the grain size of the investigated sample were studied using SEM [28]. Fig. 3 illustrates SEM micrographs of $BaCo_2Fe_{16}O_{27}$ nanoparticles. SEM images show a spongy morphology with the agglomerated grains. The average grain size of the sample is 73.7 nm. A reason for agglomeration is dipole interaction between the crystallites [29]. The grains have an irregular distribution with a hexagonal shape, which is the basic crystal cell of W- type ferrites. The EDX energy spectra of $BaCo_2Fe_{16}O_{27}$ HFs are presented in Fig. 4. The inset table in Fig. 4 illustrates the weight percentage (wt. %) and atomic percentage (at.%) of the O, Ba, Fe and Co elements theoretically and experimentally. The theoretical wt. % and at.% were calculated from the chemical formula $BaCo_2Fe_{16}O_{27}$ while the experimental values were obtained from EDX. The weight and atomic percentages

Table 1 The values of the lattice parameters a, c, the theoretical density (D_x), the unit cell volume (V), the crystallite size (D) and the molecular weight for the sample $BaCo_2Fe_{16}O_{27}$

Sample	a(Å)	c(Å)	c/a	V(Å)^3	D_x (g/cm^3)	Crystallite size (nm)	Molecular weight (g)
$BaCo_2Fe_{16}O_{27}$	6.2179	29.0580	4.6733	1123.46	3.32	37.39	1175.87

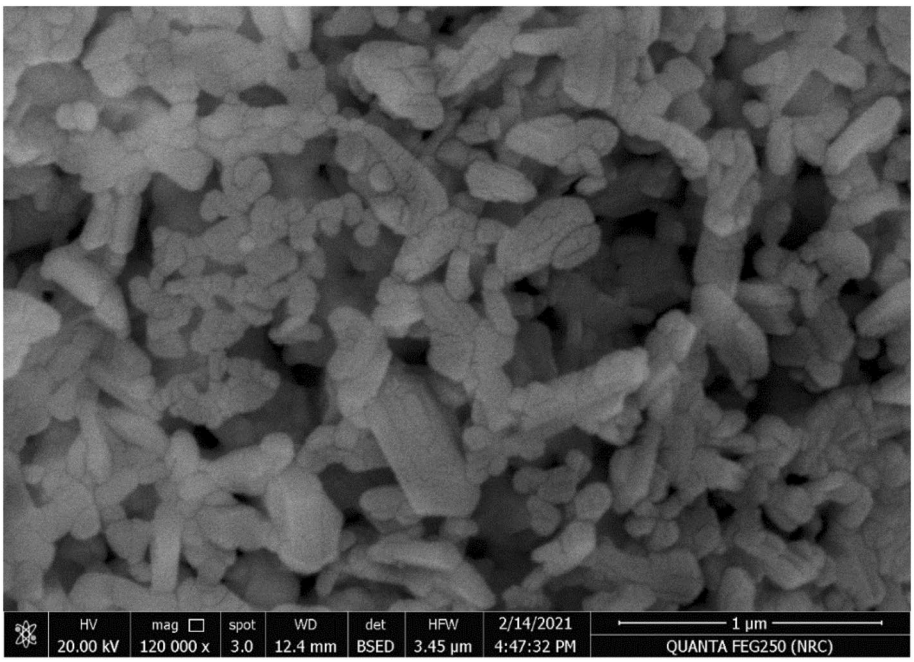

Fig. 3 SEM of the sample $BaCo_2Fe_{16}O_{27}$

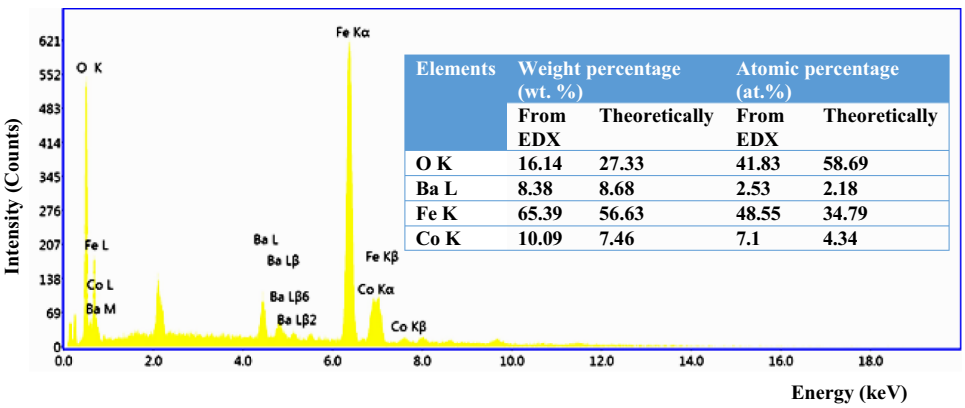

Elements	Weight percentage (wt. %)		Atomic percentage (at.%)	
	From EDX	Theoretically	From EDX	Theoretically
O K	16.14	27.33	41.83	58.69
Ba L	8.38	8.68	2.53	2.18
Fe K	65.39	56.63	48.55	34.79
Co K	10.09	7.46	7.1	4.34

Fig. 4 EDX for the investigated sample. The inset table illustrates the weight percentage (wt. %) and atomic percentage (at.%) of the O, Ba, Fe and Co elements

clearly illustrate a small variation between the experimental and theoretical values due to oxygen deficiency, which can be advantageous for heavy metal removal from water. Figure 5 illustrates the elemental mapping of $BaCo_2Fe_{16}O_{27}$ sample. The elements barium, cobalt, iron and oxygen are present in a homogenous distribution.

The magnetic properties of the investigated sample were studied using a vibrating sample magnetometer (VSM). Figure 6 (a) illustrates the curve of magnetic hysteresis for $BaCo_2Fe_{16}O_{27}$ nanoparticles at room temperature. The values of coercive field H_c, saturation magnetization M_s and remanent magnetization M_r were listed in Table 2. The saturation magnetization (M_s) was determined also by the law of approach to saturation (LAS) [30, 31]:

$$M = M_s\left(1 - \frac{A}{H} - \frac{B}{H^2}\right) + \chi H \tag{6}$$

where M_s is the saturation magnetization of the domains per unit volume, A is a constant associated with microstress, B is a constant representing the magneto-crystalline

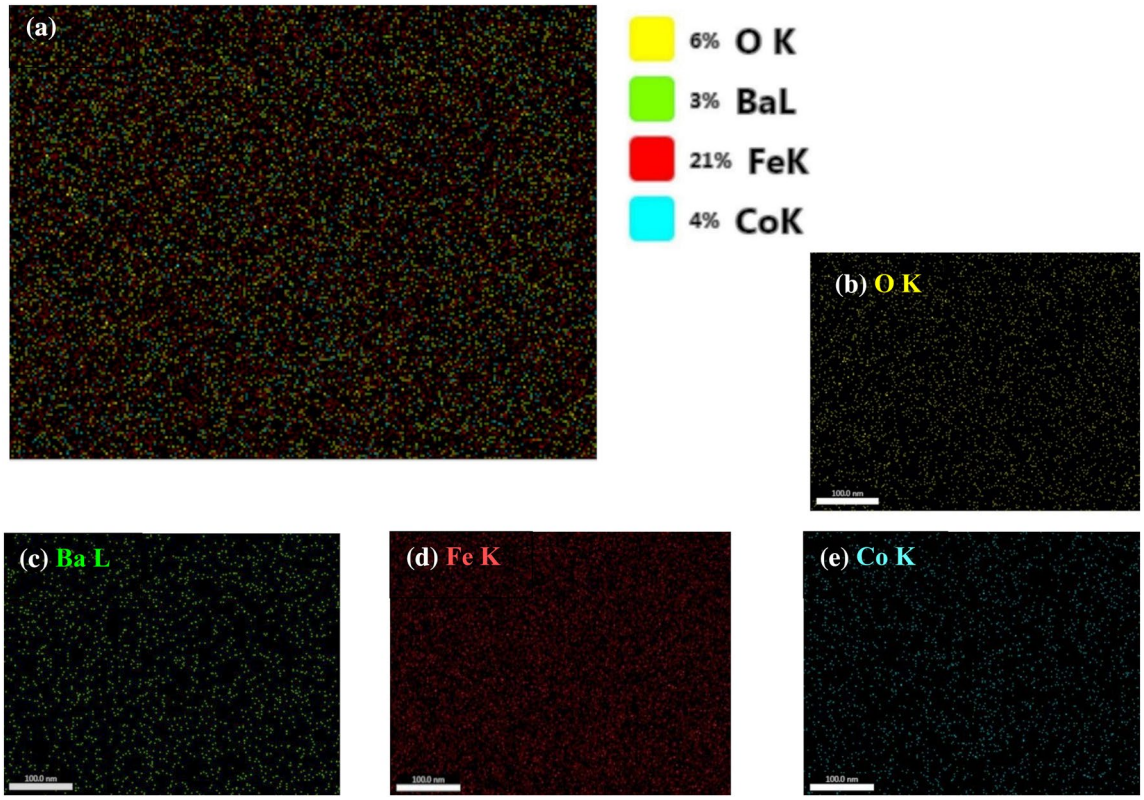

Fig. 5 The elemental mapping of $BaCo_2Fe_{16}O_{27}$ sample

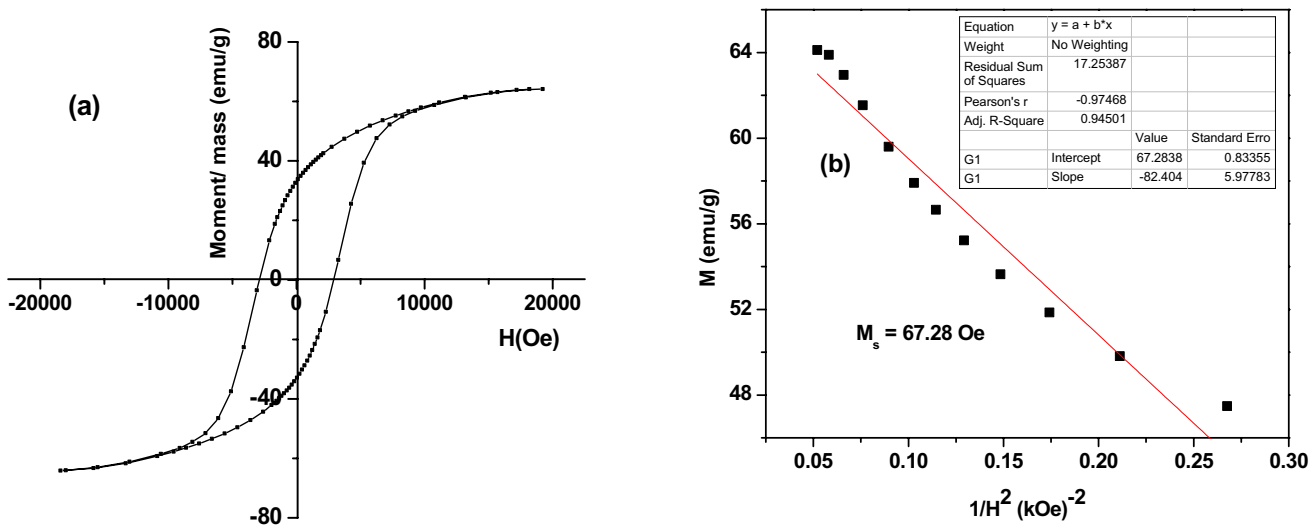

Fig. 6 **a** VSM for $BaCo_2Fe_{16}O_{27}$ sample. **b** fitting plot between M versus $1/H^2$

Table 2 Values of the saturation magnetization (M_s), remanence magnetization (M_r), the coercive field (H_c), M–H loop area, Anisotropy Constant (K) and Squareness ratio for $BaCo_2Fe_{16}O_{27}$

Sample	M_s (emu.g^{-1})	M_r (emu.g^{-1})	H_c Oe	M–H loop area (erg.g^{-1})$\times 10^3$	K (emu Oe.g^{-1})	Squareness
$BaCo_2Fe_{16}O_{27}$	64.133	33.099	2892.1	500.86	193,207	0.516

anisotropy contribution, and χH is the forced magnetization term. Figure 6 (b) illustrates the plotting of M versus $1/H^2$ in the high field range given a straight line. The saturation magnetization M_s of $BaCo_2Fe_{16}O_{27}$ nanoparticle can also be detected by extrapolating the plot of magnetization versus $1/H^2$ to approach zero [32–34]. In this method, the M_s value is 67.28 emu/g. The obtained value is very comparable to the experimental value, signifying that an applied field of ± 20 kOe is appropriate to saturate the investigated sample. The factors affected on the magnetization of W-type hexaferrite are the composition of ferrite, the distance of the Fe–O bond and the superexchange interaction through Fe^{3+}–O–Fe^{3+} [35].

Moreover, the coercivity of W-type hexaferrite is affected by many factors such as magneto-crystalline anisotropy, shape anisotropy, and saturation magnetization [36]. The magneto-crystalline anisotropy can be determined by the Stoner-Wohlfarth equation as follows [37]:

$$K = \frac{H_C \times M_S}{0.96} \tag{7}$$

where K is the magneto-crystalline anisotropy constant, M_s is the saturation magnetization and H_c is the coercive field. The saturation magnetization and the net magnetic moment of the sample depend on the presence of the magnetic ions such as Co^{2+} (3.7 μB) and Fe^{3+} (5 μB) [38].

The squareness ratio R of the remanence to the saturation magnetization (M_r/M_s) indicates the domain structure of the investigated sample. The squareness ratio R value = 0.5 is indicative of a single domain and the lower value is associated with a multidomain structure and the particles interact by magneto-static interactions [39]. In the present work, the sample $BaCo_2Fe_{16}O_{27}$ has $R > 0.5$, indicating the exchange coupled interaction between the domains.

Figure 7 illustrates the dependence of the molar magnetic susceptibility on absolute temperature as a function of the magnetic field intensities. As shown in the figure, three distinct regions were obtained. With increasing temperature, χ_M increases steadily in the first region, rapidly increased in the second region, and decreases rapidly in the third region.

A deeper examination of the first region reveals the sample to be pure ferrimagnetic material in which the thermal energy was insufficient to disturb the aligned moments of the spins. In the second region, the thermal energy is enough to make the dipoles freely align in the direction of the applied field. In the last region, the sample transfers from ferrimagnetic to paramagnetic behavior after the Curie temperature where χ_M decreases drastically.

Figure 8 shows the relation between the reciprocal of magnetic susceptibility χ_M^{-1} and the absolute temperature

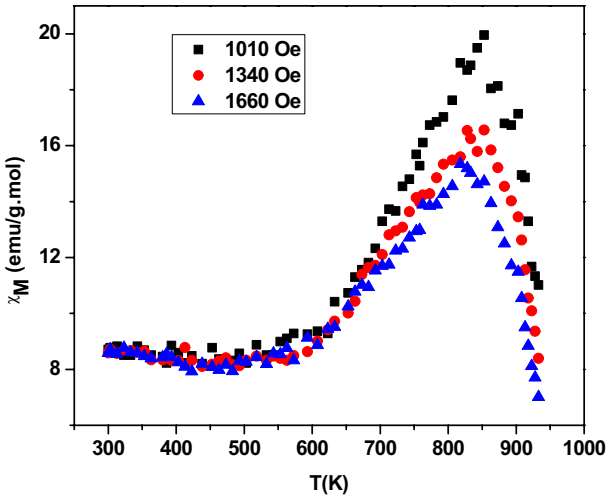

Fig. 7 The dependence of the molar magnetic susceptibility and the absolute temperature for the sample

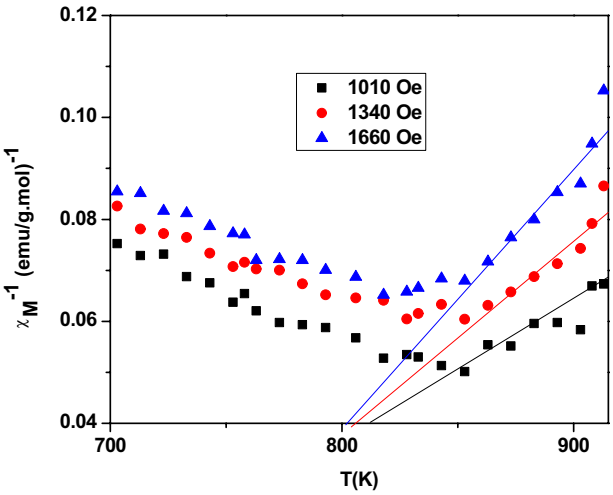

Fig. 8 Dependence of the reciprocal molar magnetic susceptibility on the absolute temperature in the paramagnetic region

at different magnetic field intensities in the paramagnetic region. The magnetic parameters, such as the Curie constant (C) and the Curie–Weiss constant (θ), were calculated from the extrapolation of the linear part χ_M^{-1} in the paramagnetic region. The Curie constant (C) equal to the reciprocal of the slope of a straight line in the paramagnetic region. The values of effective magnetic moments (μ_{eff}) were calculated from the following relationship

$$\mu_{eff} = 2.83\sqrt{C} \tag{8}$$

Table 3 Values of the Curie constant (C), the Curie–Weiss constant (θ) and the effective magnetic moment (μ_{eff}) of the sample $BaCo_2Fe_{16}O_{27}$ at different magnetic field intensities

Field (Oe)	C (emu/(g.mole)) K	θ (K)	μ_{eff} (B.M)
1010	3814.815	812	174.79
1340	2619.047	805	144.83
1660	1982.46	802	126.01

where C is the Curie constant. These magnetic parameters were reported in Table 3. The data obey the well-known Curie–Weiss law [40].

$$\chi_M = \frac{C}{(T+\theta)} \tag{9}$$

where χ_M is the molar magnetic susceptibility, T is the absolute temperature and θ is the Curie–Weiss constant. The magnetic properties of the sample $BaCo_2Fe_{16}O_{27}$ are originated from the Fe^{3+}–O–Fe^{3+} superexchange interactions, which are mutually antiparallel, and also the Fe^{3+}–Fe^{3+} direct exchange interactions.

Table 4 illustrates the comparative study between the present results and those reported earlier. The author noticed that my sample is the largest in the remanence magnetization and the coercive field, compared with the results obtained by other authors [16, 41–44]. The saturation magnetization (M_s) of the present sample is smaller than the sample obtained by Mohammad K. Dmour [42]. The variation in the values of M_s, M_r and H_c for the samples is due to the different preparation methods and ionic radii.

The investigated sample was prepared in nano scale (crystallite size = 37.39 nm) with a spongy morphology so the surface to volume ratio is large, which increases the number of active sites to trap Pb^{2+} ions and increases the removal efficiency. One of the main advantages of using $Baco_2Fe_{16}O_{27}$ for Pb^{2+} adsorption is the easy separation from the solution using an external magnetic field due to its large magnetization.

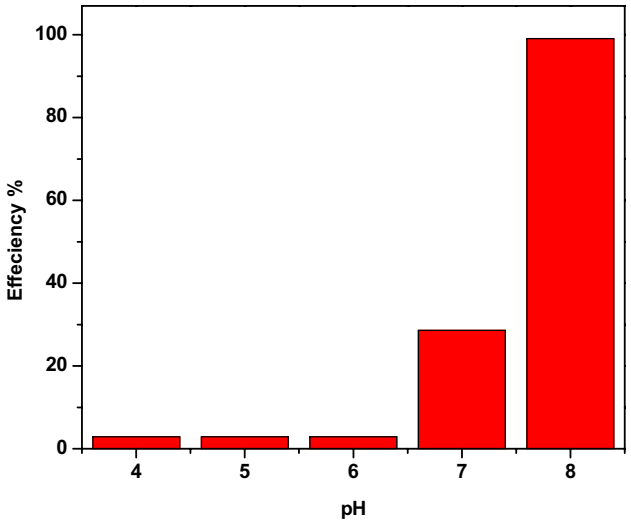

Fig. 9 Effect of pH on the adsorption efficiency of Pb^{2+} ions

The heavy metal Pb^{2+} ion removal from the wastewater was studied with different parameters such as pH value and contact time. Figure 9 illustrates the effect of pH solution on the heavy metal adsorption process. The adsorption of Pb^{2+} ion increased by increasing the pH value. It is clear that at lower values of pH, the adsorption of heavy metal ions is low. This is due to competition between H^+ and Pb^{2+} on the active sites of adsorbent [45]. At pH = 7, the amount of H^+ decreases in the solution and Pb^{2+} can be easily adsorbed on the active sites. Otherwise, at pH = 8, the solution contains oH^-. Consequently, the heavy metal Pb^{2+} can be precipitated as lead hydroxide [46]. The precipitation of Pb^{2+} at pH 8 is not only a result of the adsorption of Pb^{2+} on $BaCo_2Fe_{16}O_{27}$, but also the formation of lead hydroxide. So, the optimum pH value is 7.

The effect of contact time on the Pb^{2+} ion efficiency illustrates in Fig. 10 over a range (20–140) min. The adsorption of heavy metal Pb^{2+} increases by increasing the contact time. At the beginning of adsorption, a large number of active sites are available [47]. Finally, the optimum conditions for Pb^{2+}

Table 4 Comparative study of saturation, remanence magnetization, and coercivety for $BaCo_2Fe_{16}O_{27}$

Sample	Preparation methods	Crystallite size (nm)	M_s (emu/g)	M_r (emu/g)	Hc (Oe)	References
$BaCo_2Fe_{16}O_{27}$	Sol–gel		61.8		98.8	Huang [16]
	Solvent casting	41.24	50.31	25.49	2747	Anand [41]
	Sol–gel	415	73.03	11.42	95	Dmour [42]
	Sol–gel		71.18	8.29	151	Guo [43]
	Tartaric acid precursor	42.5	50.9	21.1	1097.6	Hessien [44]
	Citrate nitrate combustion	37.39	64.133	33.099	2892.1	The present work

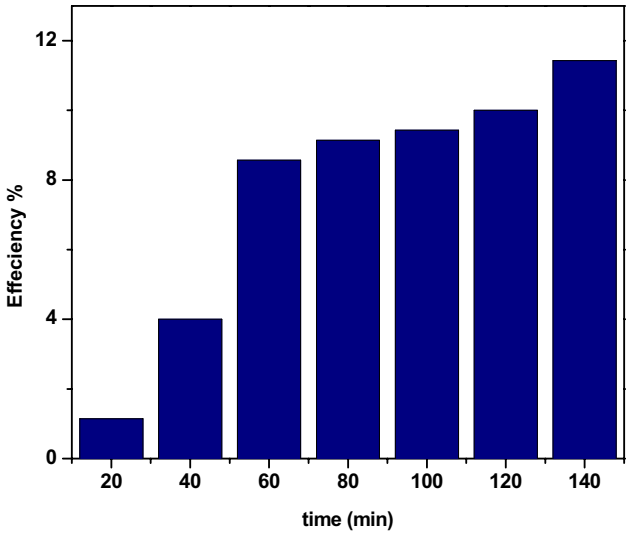

Fig. 10 Effect of contact time on the adsorption efficiency of Pb^{2+} ions

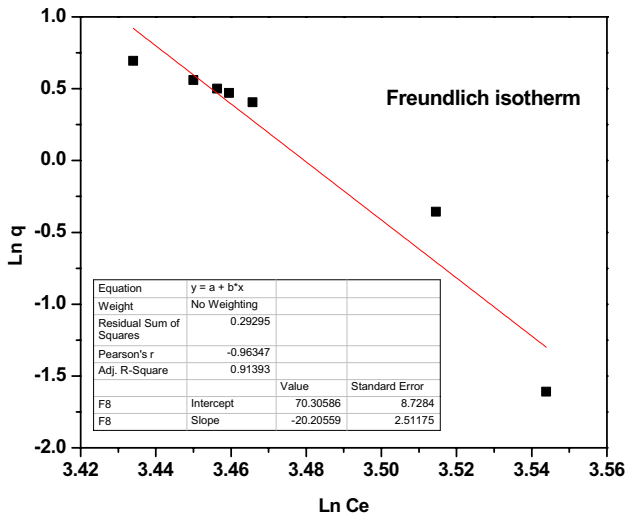

Fig. 11 Linear fit of experimental data of the adsorption of Pb^{2+} onto $BaCo_2Fe_{16}O_{27}$ according to Freundlich sorption isotherm

removal efficiency are pH 7 for 140 min using $BaCo_2Fe_{16}O_{27}$ nano particles.

The mechanism of Pb^{2+} adsorption process can be studied using the adsorption isotherm. In the present work, two isotherm models that have been studied are the Langmuir and Freundlich models.

The multilayer adsorption on a heterogeneous surface can be described by Freundlich isotherm, which is commonly used to describe heavy metal adsorption on various adsorbents. The empirical model was proven to be consistent with a heterogeneous surface's exponential distribution of active centers. The relation between the amount of solute adsorbed (q_e) and the equilibrium concentration of solute in solution (C_e) is given by the following equation:

$$q_e = K_f C_e^{\frac{1}{n}} \tag{10}$$

This equation can be linearized to give the following expression:

$$\ln q_e = \ln K_f + \frac{1}{n}\ln C_e \tag{11}$$

Where, K_f is a constant for the Freundlich system, depends on the quantity of metal ion adsorbed onto adsorbent at an equilibrium concentration. Figure 11 illustrates the dependence of ln q_e on ln C_e. The values of K_f and $1/n$ are calculated from the intercept and slope of the best fit line in Fig. 11.

The Langmuir isotherm model assumes that maximal adsorption occurs in a saturated monolayer of adsorbate molecules on the adsorbent surface. Many ground water effluent treatment procedures employ the Langmuir adsorption isotherm, which has also been used to explain the adsorption of heavy metals by various adsorbents. The Langmuir isotherm is considered that once a metal ion occupies an active site, no further adsorption occurs, and the adsorbed layer is unimolecular. The following equation describes the Langmuir isotherm model:

$$\frac{C_e}{q_e} = \frac{1}{q_m K_L} + \frac{C_e}{q_m} \tag{12}$$

where q_m is the adsorption capacity at maximum adsorption. Figure 12 shows the relation between (C_e/q_e) and (C_e) for heavy metal Pb^{2+} to determine the Langmuir constants.

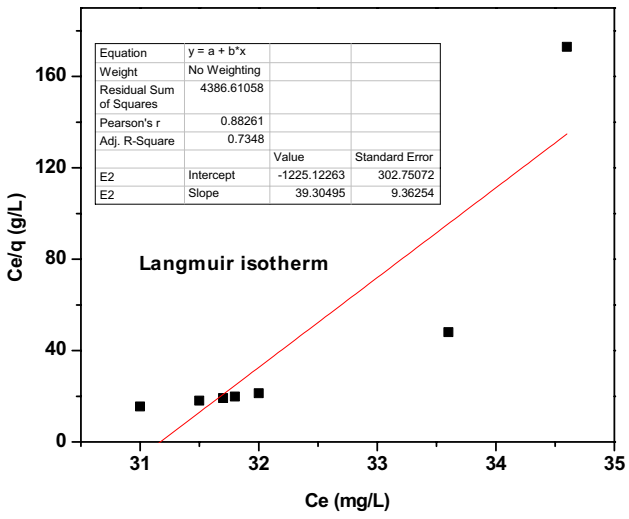

Fig. 12 Linear fit of experimental data of the adsorption of Pb^{2+} onto $BaCo_2Fe_{16}O_{27}$ using Langmuir adsorption isotherm model

By comparing the correlation coefficient R^2, the applicability of the isotherm equations is determined. The inset tables in both Figs. 11 and 12 illustrate that $R^2 = 0.91393$ for Freundlich isotherm, while $R^2 = 0.7348$ for Langmuir isotherm. Thus, the Freundlich adsorption isotherm fitted the experimental data well.

4 Conclusion

The barium hexaferrites was synthesized using citrate nitrate combustion method. XRD revealed that the sample $BaCo_2Fe_{16}O_{27}$ was crystallized in a single phase hexagonal structure with space group $P6_3/mmc$. The average crystallite size is 37.39 nm. The morphology and the grain size of the investigated sample were studied using SEM. The sample has a spongy morphology with the agglomerated grains. The average grain size of the sample is 73.7 nm. The magnetic properties of $BaCo_2Fe_{16}O_{27}$ were studied using two techniques: H–M hysteresis loop and the DC magnetic susceptibility. The sample has antiferromagnetic properties. The values of the saturation magnetization (M_s) and remanence magnetization (M_r) are 64.133 and 33.099 emu.g^{-1} respectively. The squareness ratio (M_r/M_s) is greater than 0.5, indicating the exchange coupled interaction between the magnetic domains. The heavy metal Pb^{2+} ion removal from the wastewater was studied with different parameters such as pH value and contact time. $BaCo_2Fe_{16}O_{27}$ has Pb^{2+} removal efficiency 99% and 28% at pH 8 and 7 respectively. The Langmuir and Freundlich isotherms were used to analyze the experimental data. The Freundlich adsorption isotherm fitted the experimental data well.

Funding Open access funding provided by The Science, Technology & Innovation Funding Authority (STDF) in cooperation with The Egyptian Knowledge Bank (EKB).

Declarations

Conflict of interest The author declares that he has no conflict of interest.

References

1. Z.W. Li, G.Q. Lin, L. Chen, Y.P. Wu, C.K. Ong, J. Appl. Phys. **98**, 94310 (2005)
2. Z. Su, Y. Chen, B. Hu, A.S. Sokolov, S. Bennett, L. Burns et al., J. Appl. Phys. **113**, 1 (2013)
3. Z.H. Yang, Z.W. Li, Y.H. Yang, Mater. Chem. Phys. **144**, 568 (2014)
4. H. Cho, S. Kim, Ceram. Int. **45**, 9406 (2019)
5. R. Sagayaraj, T. Dhineshkumar, A. Prakash, S. Aravazhi, G. Chandrasekaran, D. Jayarajan et al., Chem. Phys. Lett. **759**, 137944 (2020)
6. S.K. Nandi, S.K. Nath, A.K.M.A. Hossain, J.U. Khan, J. Supercond. Nov. Magn. **27**, 2655 (2014)
7. X.F. Yang, Q. Jin, Z. Chen, Q. Li, B. Liu, J. Magn. Magn. Mater. **367**, 64 (2014)
8. M.A. Khan, F. Hussain, M. Rashid, A. Mahmood, S.M. Ramay, A. Majeed, J. Mag. Mag. Mater. **452**, 73 (2018)
9. A. Awadallah, S.H. Mahmood, Y. Maswadeh, I. Bsoul, M. Awawdeh, Q.I. Mohaidat et al., Mater. Res. Bull. **74**, 192 (2016)
10. T. Koutzarova, S. Kolev, I. Nedkov, K. Krezhov, D. Kovacheva, B. Blagoev et al., J. Supercond. Nov. Magn. **25**, 2631 (2012)
11. M.J.P. Asl, A. Ghasemi, G.R. Gordani, J. Supercond. Nov. Magn. **28**, 109 (2015)
12. K.C. Patil, S.T. Aruna, T. Mimani, Solid State. Mater. Sci. **6**, 507–512 (2002)
13. S. R. Jain, K. C. Adiga, V. R. Pai Verneker, Combustion and flame **40,** 71–79 (1981).
14. A. Majid, J. Tunney, S. Argue, D. Wang, M. Post, J. Alloys Compd. **398**, 48–54 (2005)
15. A. Mali, A. Ataie, Ceram. Int. **30**, 1979–1983 (2004)
16. K. Huang, X. Liu, S. Feng, Z. Zhang, J. Yu, Niu, X. Huang et al., J. Magn. Magn. Mater. **379,** 16–21 (2015).
17. M.A. Ahmed, N. Okasha, R.M. Kershi, J. Magn. Magn. Mater. **320**, 1146–1150 (2008)
18. J. Tang, X. Liu, K.M.U. Rehman, D. Li, M. Li, Y. Yang, J. Magn. Magn. Mater. **452**, 354–359 (2018)
19. T. Ahamad, M. Naushad, B. M. Al-Maswari, J. Ahmed, Z. A. ALOthman, S. M. Alshehri et al. J. Ind. Eng. Chem. **53,** 268 (2017).
20. H. Sadegh, G.A.M. Ali, V.K. Gupta, A.S.H. Makhlouf, R.S. ghoshekandi, M.N. Nadagouda et al. J. Nanostruct. Chem. **7,** 1 (2017).
21. D. Pal, S.K. Maiti, Environ. Saf. **187**, 109833 (2020)
22. X. Wang, Y. Guo, L. Yang, M. Han, J. Zhao, X. Cheng et al., J. Anal. Toxicol. **2**, 154 (2012)
23. A. Tripathi, M.R. Ranjan, J. Bioremed. Biodeg. **6**, 315 (2015)
24. M.M. Arman, N.G. Imam, R.L. Portales, S.I. El-Dek, J. Magn. Magn. Mater. **513**, 167097 (2020)
25. R. Ramadan, S.I. El-Dek, M.M. Arman, Appl. Phys. A. **126**, 900 (2020)
26. M.M. Arman, S.I. El-Dek, J. Phys. Chem. Solids **152**, 109980 (2021)
27. M. Reda, S.I. El-Dek, M.M. Arman, J. Mater. Sci. **33**(21), 16753–16776 (2022)
28. E.E. Ateia, M.A. Ateia, M.G. Fayed, S. El-Hout, S.G. Mohamed, M.M. Arman, Appl. Phys. A **128**, 1–10 (2022)
29. A. Ghasemi, S. Ekhlasi, M. Mousavinia, J. Mag. Mag. Mater. **354**, 136 (2014)
30. S.H. Mahmood, G.H. Dushaq, I. Bsoul et al., J. Appl. Math. Phys. **2**, 77 (2014)
31. D. Jiles, Introduction to Magnetism and Magnetic Materials, 3rd ediition. (CRC Press, 2015)
32. A. Baykal, S. Esir, A. Demir, S. Güner, Ceram. Int. **41**, 231 (2015)
33. M.A. Almessiere, Y. Slimani, A. Baykal, Ceram. Int. **44**, 9000 (2018)

34. S. Güner, M. Amir, M. Geleri, M. Sertkol, A. Baykal, Ceram. Int. **41**, 10915 (2015)
35. X.S. Liu, W. Zhong, S. Yang, Z. Yu, B.X. Gu, Y.W. Du, J. Magn. Magn. Mater. **238**, 207 (2002)
36. B. K. Rai, S. R. Mishra, V. V. Nguyen, J. P. Liu J. Alloys Compd. **550,** 198 (2013).
37. E.E. Ateia, M.M. Arman, E. Badawy, Appl. Phys. A **125**, 499 (2019)
38. R.A. Khan, S. Mizukami, A.M. Khan, B. Ismail, A.R. Khan, T. Miyazaki, J. Alloys Compd. **637**, 197 (2013)
39. J.C. Jiles, Acta Materiala. **51**, 5907 (2003)
40. M.M. Arman, M.A. Ahmed, Appl. Phys. A **1–9**, 128 (2022)
41. S. Anand, S. Pauline, Adv. Mater. Interf. **8**(3), 2001810 (2021)
42. M. K. Dmour, E. S. Al-Hwaitat, I. Bsoul, S. H. Mahmood J. Superconductivity Novel Magn. **33(2)**, 473–482 (2020).
43. F. Guo, X. Wu, G. Ji, J. Xu, L. Zou, S. Gan, J. Supercond. Novel Magn. **27**(2), 411–420 (2014)
44. M.M. Hessien, D.A. Rayan, M.H.H. Mahmoud, A. Alhadhrami, M.M. Rashad, J. Mater. Sci. **29(12),** 9771–9779 (2018).
45. Y. Kikuchi, Q. Qian, M. Machida, H. Tatsumoto, Carbon **44**, 195 (2006)
46. M.A. Ahmed, S.T. Bishay, S.M. Abd-Elwahab, R. Ramadan, J. Mol. Liq. **240**, 604 (2017)
47. S.Z.N. Ahmad, W.N.W. Salleh, A.F. Ismail, N. Yusof, M.Z.M. Yusop, F. Aziz, Chemosphere **248**, 126008 (2020)